ACS APPLIED MATERIALS & INTERFACES

Research Article

www.acsami.org

Facile and Economical Synthesis of Large Hollow Ferrites and Their Applications in Adsorption for As(V) and Cr(VI)

Jingna Dui, Gongyu Zhu, and Shaomin Zhou*

Key Lab for Special Functional Materials of Ministry of Education, Henan University, 475004 Kaifeng, P. R. China

Supporting Information

ABSTRACT: Unlike the previous ferrites (MFe_2O_4; M = Fe, Co, Zn, and Mn) solid nanospheres/nanoparticles, which were prepared by polluted solvothermal (glycol) approaches, here controllable monodisperse porous ferrites hollow nanospheres are promptly synthesized by a nontemplate hydrothermal method which has introduced an addition agent, polyacrylamide. The hollow nanospheres with different size can be prepared by varying the synthetic compositions. Scanning/transmission micros-graphs show the outside diameters of ferrite nanospheres are 180−380 nm and the shell thicknesses of that are only 20−45 nm, which could be adjusted by controlling CH_3COONa concentration. X-ray diffraction (XRD) and X-ray photoelectron (XPS) spectroscopy, scanning electron (SEM) and transmission electron (TEM) microscopy, energy-dispersive spectrometer (EDS), the measurement of N_2 adsorption−desorption isotherms and Brunauer−Emmett−Teller (BET) surface area, and superconducting quantum interference device (SQID) magnetometer were adopted to analyze their phase composition, morphology, porosity, and magnetic properties, respectively. The results of controlled experiments show that citrate and polyacrylamide are vital for the phase purities and morphology of ferrites. In particular, the as-obtained samples exhibit a large adsorption capacity for the toxic solution containing As(V) and Cr(VI) ions, and the calculated result of the maximum adsorption capacity is 340 mg/g based on Langmuir model, which shows excellent As(V) and Cr(VI) ions uptake capacity in contrast to other solid nanosphere materials.

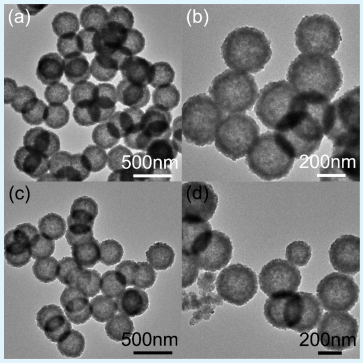

KEYWORDS: *As(V) and Cr(VI) ions, hollow nanospheres, ferrites, mesoporous, absorption*

INTRODUCTION

After silica hollow spheres were prepared by Caruso in 1998,[1] nanostructure materials with hollow interior have attracted steadily growing attention since they always show some qualities which can be substantially different from solid structures, including high specific surface area, good stability, different magnetic property, and excellent optical property. Up to now, Sb_2S_3, TiO_2, SnO_2, SiO_2, MnO_2, Fe_3O_4, and Cu_2O hollow structures have been fabricated.[2−10] Among these hollow structures, magnetic hollow nanospheres become a particularly significant field of investigation because that they have some potential applications in many areas, such as drug delivery, catalyst, high-density magnetic data storage, magneto-fluid, spin electronic devices, magnetic resonance imaging, and electrophotographic developers.[11−13] Recently, representative Fe_3O_4 hollow spheres become the focus of research and have extensively been synthesized by various approach-es[14−16]because of their high natural abundance, environmental benignity, low cost, and high theoretical capacity.[17] However, these materials were generally synthesized under high temper-ature and high pressure using autoclaves, which hampers economical large-scale production. Chen and Yu et al.[18] have synthesized porous hollow Fe_3O_4 beads for lithium ion battery anodes via a solvothermal route, which is not enough friendly to the environment. α-Fe_2O_3 nanospheres, which had the orphology of sheet-like subunits were obtained via the hydrothermal route,[19] however, the method is compex and difficult to control in size because that the soft templates of oil-in-water quasiemulsion microdroplets for the deposition of products is difficult to control the uniformity of the microdroplets shell. A hydrothermal and calcinated route was used to synthesize flowerlike Fe_3O_4 nanospheres with hollow interior structures,[20] whereas the hollow structures of that is little but irregular. Zhu, Lu-Ping, et al.[21] promoted a route for the fabrication of Fe_3O_4 hollow spheres, nevertheless the reactant ethylenediamine is harm to the environment. So far, there are few reports on hydrothermal synthesis of mono-disperse ferrites nanospheres (MFe_2O_4; M = Fe, Co, Zn, and Mn) with large hollow structures, high water solubility, high saturation magnetization, and environment friendly.

In this paper, we aimed to propose a current hydrothermal reduction route for the synthesis of hydrophilic, mesoporous, and easily dispersed ferrites with a large hollow structure by modifying the reaction to prepare porous Fe_3O_4 hollow nanospheres whose hollow structures are not enough large,[22] and we can control the diameters and the shell thicknesses of mesoporous ferrites hollow nanospheres by changing the dosage of CH_3COONa. This work will promote a significant

Received: July 4, 2013
Accepted: September 25, 2013
Published: September 25, 2013

route for synthesizing magnetic, mesoporous and easily dispersed hollow nanospheres, and provide a process to promising applications about the hollow nanospheres. There is no doubt that the magnetite promotes quick separation process of the As(V) and Cr(VI) ions from the wastewater by an external magnetic field, which has a high saturation magnetization. Due to the highly porous structure, high surface area, high-quality monodisperse, and high magnetic saturation of the prepared ferrites, the hollow nanospheres used as adsorbent for wastewater containing As(V) and Cr(VI) ions exhibit a superior adsorption capacity in removing diverse pollutants.

EXPERIMENTAL SECTION

Ferric chloride hexahydrate ($FeCl_3{\cdot}6H_2O$), sodium citrate ($C_6H_5Na_3O_7{\cdot}2H_2O$), sodium acetate ($CH_3COONa$), manganese chloride tetrahydrate ($MnCl_2{\cdot}4H_2O$), anhydrous zinc chloride ($ZnCl_2$), polyacrylamide (PAM), sodium arsenate ($Na_3AsO_4{\cdot}12H_2O$), potassium dichromate ($K_2Cr_2O_7$), and cobalt chloride hexahydrate ($CoCl_2{\cdot}6H_2O$) are analytical grade reactants and then used with no further disposal. Iron standard solutions for Inductively Coupled Plasma (ICP) tests were acquired from Sinopharm Group Chemical Reagent Co., Ltd. with analytic grade and adopted as supplied. To simulate the wastewater from an electronics corporation, Henan, China, As(V)−Cr(VI) solution was obtained by dissolving $Na_3AsO_4{\cdot}12H_2O$ and $K_2Cr_2O_7$ in ultrapure water and the As^{5+}/Cr^{6+} concentration were ∼7200/1800 μg/L which were same as the wastewater.

The synthesis of mesoporous Fe_3O_4 hollow nanospheres: In a typical reaction, 1.5 mmol $FeCl_3{\cdot}6H_2O$, 3 mmol $C_6H_5Na_3O_7{\cdot}2H_2O$, and 4.5 mmol CH_3COONa were dissolved in 30 mL deionized water obtaining a laurel-green transparent solution, after added 0.3 g of PAM. The mixture solution was stirred vigorously about 0.5 h until the PAM dissolved totally. The solution was then sealed in two Teflon-lined stainless-steel autoclave (20 mL capacity) averagely and placed in an oven at 180 °C for 12 h, and then, was cooled to room temperature naturally. The black precipitate was collected and ultrasonic washed for several times with deionized water or ethanol, totally. The yielded product was vacuum-dried at 60 °C for 6 h.

According to the above synthesis progress, the possible chemical reactions in this system are proposed as follows:

$$CH_3COONa + H_2O \rightleftharpoons CH_3COOH + OH^- + Na^+$$

$$-(OCCH_2)_2C(OH)CO- + Fe^{3+} \longrightarrow -(OCCH_2)_2C{=}O + Fe^{2+} + CO_2 + H^+$$

$$Fe^{3+} + 3OH^- \longrightarrow Fe(OH)_3$$

$$Fe^{2+} + 2OH^- \longrightarrow Fe(OH)_2$$

$$2Fe(OH)_3 + Fe(OH)_2 \longrightarrow Fe_3O_4 + 4H_2O$$

The above route could be used to the manufacture of MFe_2O_4 (M = Co, Zn, and Mn) ferrites hollow nanospheres by coprecipitating the chlorides of M^{2+} and Fe^{3+} (M^{2+}/Fe^{3+} = 0.5). Taking the sample of $CoFe_2O_4$ as an example, a mixture solution of $CoCl_2{\cdot}6H_2O$ (0.1730 g, 0.5 mmol) and $FeCl_3{\cdot}6H_2O$ (0.3780 g, 1 mmol) under the same reaction conditions like the synthesis of porous Fe_3O_4 hollow nanospheres, produced mesoporous hollow nanospheres of $CoFe_2O_4$.

The X-ray diffraction (XRD) patterns of the MFe2O4 were obtained by adopting Philips X Pert Pro diffractometer with Cu Kα (λ = 1.54056 Å) radiation to characterize the crystalline phase of the products. Energy-dispersive spectrometer (EDS) from individual ferrite nanosphere analysis was carried out to characterize the chemical composition of the as-obtained samples. X-ray photoelectron spectroscopy [XPS (AXIS ULTRA XPS, Al Kα)] was also carried out to characterize chemical composition and value of the ferrite products. The sizes and morphologies of the as-obtained hollow nanospheres were characterized by adopting scanning electron microscopy (SEM, JSM5600LV) and transmission electron microscopy (TEM, JEOL2010). The porosity and specific surface areas of the yielded hollow spheres was substantiated by adsorption−desorption of ultrapure N_2 on a Quantachrome Instruments system via Brunauer−Emmett−Teller (BET) method surface area. The magnetic properties of the product were investigated using a superconducting quantum interference devices magnetometer (SQID, MPMS XL7).

Ferrite hollow nanospheres (MFe_2O_4; M = Fe, Co, Zn, and Mn) for adsorption tests were 10 mg/L, respectively. The concentration of heavy metal As(V) and Cr(VI) ions was changed by diluting original wastewater with deionized water, and pH of the solutions would be modulated by 0.1 M NaOH or HNO_3 solutions. Adsorption tests were carried out by mixing the 380 nm ferrites hollow nanospheres with the wastewater. Meanwhile, the mixture solutions were agitated at 250 rpm in an ultrasonic cleaner at 25 ± 2 °C. After a specified time, the solid and liquid were magnetic separated. Adsorption isotherm studies were acquired by adjusting the initial heavy metal As(V) and Cr(VI) ions concentration (400−9000 ug/L) and the solution pH (= 3, 5, 7 and 9). When the equilibrium of the adsorption was reached, the adsorbent was separated by a magnet which is similar to the recycling Fe_3O_4/C particles[23]and in order to execute the metal analysis, the supernatant was got together. The concentration of iron, As(V) and Cr(VI) ions was carried out by an inductively coupled plasma-optical emission spectrometer (ICP-OES, Optima 3200XL, PerkinElmer). Iron concentration was determined through the International Standard (ISO 11885:1997), but for As(V) and Cr(VI) ions measurement, continuous flow hydride generation combined (PerkinElmer) with ICP were employed to amend the sensitivity of the evaluation. All the experimental data were the average of double determinations.

The Langmuir isotherm models are used to simulate As(V) and Cr(VI) ions adsorption onto magnetic hollow nanospheres. The adsorption capacity (q_e) was calculated according to the model expressed as follows:

$$q_e = (C_{0C} - C_{eC})V/m$$

where q_e (mg/g) is the adsorption ability of magnetic nanospheres; C_{0C} and C_{eC} represents the initial and equilibrium concentration of As(V) and Cr(VI) ions in solution, respectively; V (mL) is the volume of the supernate; and m (mg) is the adsorption amount for As(V) and Cr(VI) ions.

RESULTS AND DISCUSSION

The structures of the as-prepared ferrites were investigated by XRD analysis showed in Figure 1. The typical γ-Fe_2O_3 (JCPDS Card No. 39-1346) peaks do not appear in the as-obtained XRD patterns such as (110), (210), and (211) and all peaks of

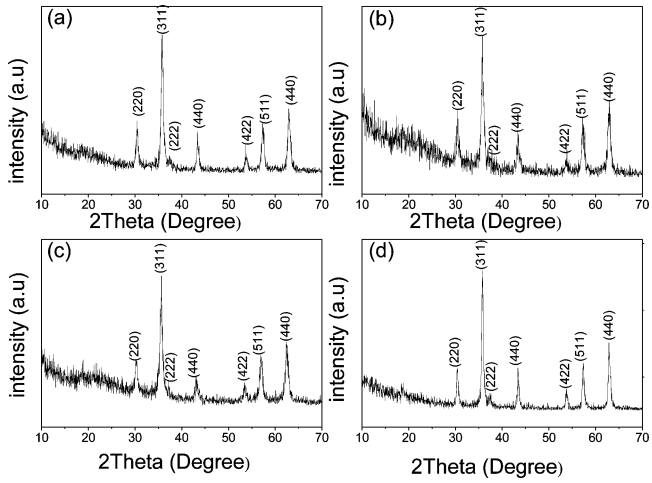

Figure 1. XRD patterns of Fe_3O_4 (a), $CoFe_2O_4$ (b), $ZnFe_2O_4$ (c), and $MnFe_2O_4$ (d).

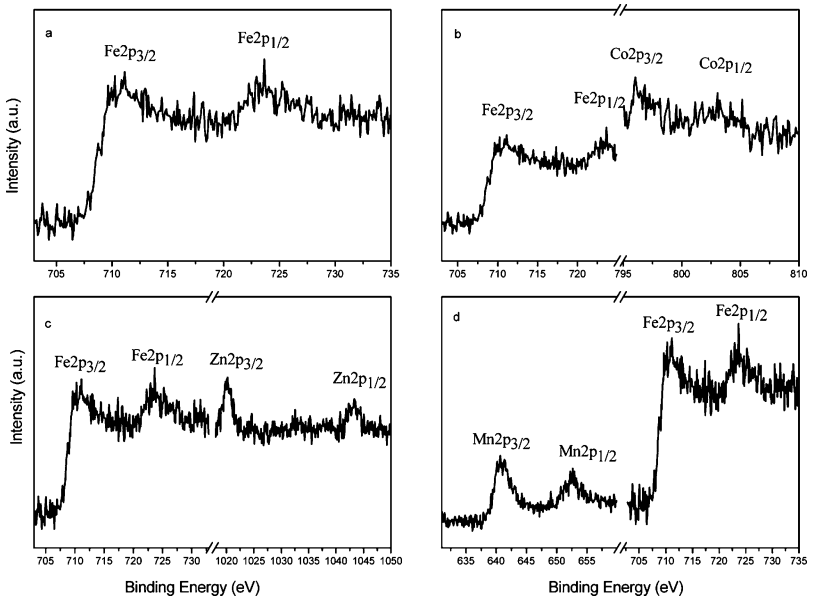

Figure 2. XPS patterns of the as-prepared Fe_3O_4 (a), $CoFe_2O_4$ (b), $ZnFe_2O_4$ (c), and $MnFe_2O_4$ (d).

a, b, c, and d match well with standard Fe_3O_4 (JCPDS Card No. 75-1610), $CoFe_2O_4$ (JCPDS Card No. 22−1086), $ZnFe_2O_4$ (JCPDS Card No. 22-1012), and $MnFe_2O_4$ (JCPDS Card No. 74-2403), respectively. According to the Scherrer formula, the average crystallite sizes calculated were approximately 20, 17, 16, and 16 nm, respectively, based on the strongest peaks (311) and much smaller than outer diameters (180−380 nm) of these hollow nanospheres which will be discussed below.

EDS from individual ferrite nanosphere analysis was carried out to determine the chemical composition of the hollow nanospheres (See Supporting Information Figure S1), too. Besides the Cu peaks which come from the copper grids, only Fe and O peaks appear in the sample of Fe_3O_4 (Supporting Information Figure S1a); Co, Fe and O peaks appear in the sample of $CoFe_2O_4$ (Supporting Information Figure S1b); Zn, Fe, and O peaks appear in the sample of $ZnFe_2O_4$ (Supporting Information Figure S1c); and Mn, Fe, and O peaks appear in the sample of $MnFe_2O_4$ (Supporting Information Figure S1d). Further quantitative analyses of EDS indicate that the Fe/O atomic ratio of 3:4 observed for the sample of Fe_3O_4 and for each of the other three MFe_2O_4 products (M =Co, Zn, and Mn) an analogous atomic ratio of M/Fe/O is about 1:2:4, matching well with the results of above XRD patterns and the expected stoichiometry in each case.

To better analyze the as-prepared nanostructures of MFe_2O_4, We also carried out a detailed analysis of their electronic states. The purity of four products was determined by the XPS [Figure 2; XPS patterns of the as-prepared Fe_3O_4 (a), $CoFe_2O_4$ (b), $ZnFe_2O_4$ (c), and $MnFe_2O_4$ (d)], in which XPS patterns of Fe_3O_4 and $CoFe_2O_4$ are compatible with our previous work.[24,25] The binding energy range from 0 to 1000 eV in Figure 2. Compared with the standard XPS spectra of that, we can see that besides the binding energy peak of element C, the as-prepared samples contained only the three element types of elements M, Fe, and O, which has not found other peaks of impurity elements, indicating the synthesized samples are much pure, agreement with the above outcomes of XRD and EDS patterns. The XPS spectra of the as-prepared samples of Fe_3O_4 (Figure 2a) at 710.3 and 723.7 eV nearby were attributed to the two peaks of $Fe2p_{3/2}$ and $Fe2p_{1/2}$, respectively, consistent with the report data in the literature of Fe_3O_4 XPS, demonstrating that the synthesized sample was a single phase of Fe_3O_4. Figure 2b corresponds the high-resolution XPS spectra of Co2p and Fe2p. In the Figure 2b, besides the two peaks of $Fe2p_{3/2}$ and $Fe2p_{1/2}$, there is a distinct peak recorded at 780.8 eV in the spectrum of Co2p, which corresponds to the $Co2p_{3/2}$, whose satellite peak is at 785.9 eV. In addition, the peak of $Co2p_{1/2}$ is at 797.2 eV, whose corresponding satellite peak is at 803.0 eV, where the two peaks of 780.8 and 797.2 eV are major peaks and their corresponding satellite peaks are attributed to the two high spin states of Co^{2+}, indicating that the as-obtained $CoFe_2O_4$ is single phase. Most of the quantitative analysis of the XPS spectrum translates the ratio of the peak intensity of each spectrum measured in the experiment into the elements content ratio, namely transforms the corresponding peak area to the amount of elements. Because the measured $CoFe_2O_4$ ingredients of XPS spectra always exist the absorption of oxygen, it is impossible to determine the composition ratio of oxygen element, but the ratio between the element Fe and Co is constant. After analysis, the atomic ratio of Co and Fe in our samples is about 1:2, consistent with the results of EDS pattern mentioned above. Meanwhile, in the Figure 2c and 2d, besides the two peaks of $Fe2p_{3/2}$ and $Fe2p_{1/2}$, two major peaks at 1020.1 and 1043.4 eV (Figure 2c) are attributed to the Zn $2p_{3/2}$ and the Zn $2p_{1/2}$, respectively, and two major peaks at 640.6 and 652.7 eV (Figure 2d) are attributed to the Mn $2p_{3/2}$ and the Mn $2p_{1/2}$, respectively. Furthermore, the atomic ratio of Zn (Mn) and Fe in our samples is also about 1:2, consistent with the results of EDS pattern discussed above.

TEM and SEM were conducted for examining the morphologies and sizes of as-obtained hollow nanospheres, as shown in Figure 3(Figure 3a for Fe_3O4; Figure 3b for $CoFe_2O_4$; Figure 3c for $ZnFe_2O_4$; Figure 3d for $MnFe_2O_4$) and Figure S2 [see Supporting Information S2 for SEM images of the hollow nanospheres Fe_3O_4 (a), $CoFe_2O_4$ (b), $ZnFe_2O_4$ (c), and $MnFe_2O_4$ (d)]. Both of the TEM and SEM images show the as-obtained productions compose of a high yield of uniform ferrites nanospheres whose average diameter is about 380 nm. Moreover, the strong electron density contrasted between dark edge and pale center proves the existence of

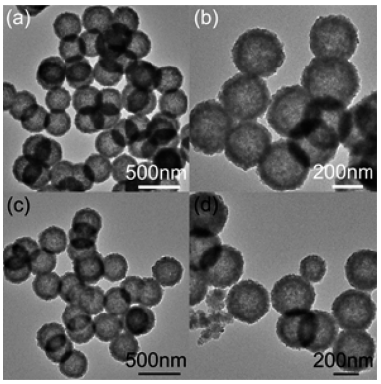

Figure 3. TEM images Fe_3O_4 (a), $CoFe_2O_4$ (b), $ZnFe_2O_4$ (c), and $MnFe_2O_4$ (d).

hollow nanostructure. Further, 40 nanospheres (Figure 3a) have been adopted for the investigation of shell thickness by computer software (SemFore 4.0). The average shell thickness is about ~45 nm. After all, both of the TEM and SEM images indicate that the as-obtained ferrites are monodisperse porous ferrites with large hollow structure. As we all know, hollow spheres ofen are fabricated by a general template-based synthesis method, and the as-fabricated hollow spheres often have a rather thin shell thickness of 20−45 nm.[7] Here even though without using any other material as a template, the monodisperse ferrites hollow nanospheres with the shell thickness of 45 nm are synthesized by simply hydrothermal method, which is undoubtedly an important progress in the synthesis of nanospheres with obvious hollow structure.

More detail structure information of one single $CoFe_2O_4$ hollow nanosphere is provided by TEM analysis (Figure 4a), in

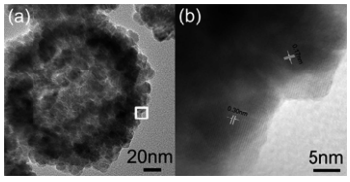

Figure 4. HRTEM image of $CoFe_2O_4$: a single hollow sphere (a) and lattice fringes (b).

which outer diameter of the hollow sphere is ~180 nm, whereas the shell thickness is ~20 nm. We can see that the hollow sphere is loosely consisted of many irregular primary nanoparticles (the diameter of ~15 nm), which indicates the ferrites are porous and polycrystalline hollow nanospheres. A typical high-resolution TEM (HRTEM) micrograph taken from the white square area in the TEM was shown in Figure 4b, from the figure it can be seen that the existent of pore structures, which is connected with the middle hollow structure, and the interplanar crystal spaceings (0.17 and 0.30 nm) are respectively marked in Figure 4b, in agreement with the interplanar distance of (422) and (220) lattice planes from XRD data mentioned above.

The specific surface areas (a) and porosity (b) of the yielded products was substantiated by the measurement of nitrogen adsorption−desorption isotherms as shown in Supporting Information Figure S4. The isotherm could be classified as style IV with a distinct hysteresis loop in the range from 0.5 P/P_0 to 1.0 P/P_0, indicating the existence of mesopores. Measured by the BET route, there is only a single peak in the mesoporus range (5−15 nm) with a dominant peak around 11.31 nm in the plot of pore size distribution. The results above can be ascribed to the interspaces of the primary particles. BET surface area of the as-obtained spheres is about 280 m^2/g which is much larger than the value for magnetite hollow spheres reported in the literature (56.7 m^2/g).[22] The pore volume is 1.23 cm^3/g. The higher specific surface area and larger pore volume further certificate that the ferrite spheres have large porous structure.

The magnetic properties of the mesoporous ferrites hollow nanospheres (~380 nm) were measured by examining the magnetic hysteresis loops at room temperature by the MPMS in the applied field sweeping from −5000 to 5000 Oe, as shown in Figure 5. The magnetic saturation values (Ms) are 89.7 emu/

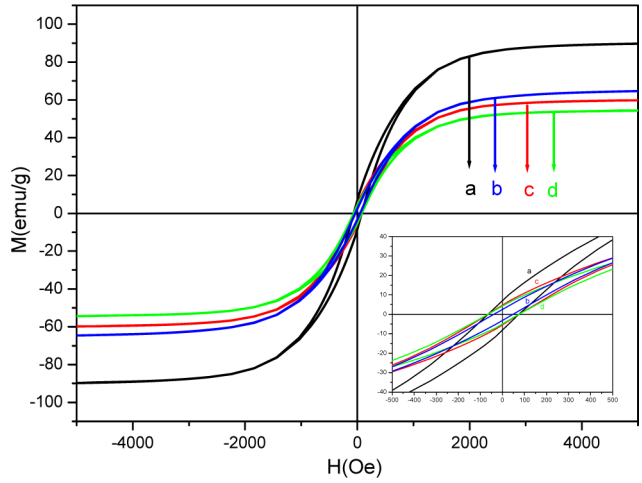

Figure 5. Magnetization curves of hollow nanospheres (outer diameter ~380 nm) at 300 K: Fe_3O_4 (a), $CoFe_2O_4$ (b), $MnFe_2O_4$ (c), and $ZnFe_2O_4$ (d). Insert: enlarged curve around zero field with a scale ranging from −500 to 500 Oe.

g for Fe_3O_4 (trace a), 64.7 emu/g for $CoFe_2O_4$ (trace b), 59.8 emu/g for $MnFe_2O_4$ (trace c), and 54.4 emu/g for $ZnFe_2O_4$ (trace d). It is noticeable that the Ms of $MnFe_2O_4$ is larger than that of $ZnFe_2O_4$, which is different with the report by Li et al,[5] but consistent with the earlier literature.[26] This result can be explained by the connection between the magnetic properties and the occupancy of cations on tetrahedral (A-site) and octahedral (B-site) sites. As we all know, Zn^{2+}(3d10) is a diamagnetic ion which ofen occupys A-site, Mn^{2+} (3d5) is a paramagnetic ion and can occupy both the two sites.[27,28] Generally, magnetite particles with sizes below 30 nm can have superparamagnetic properties.[29,30] Here the sizes of mesoporous hollow spheres are more than 380 nm (is tenth of magnetite particles' sizes) still exhibit ferromagnetic behavior, which can be caused by magnetic ordering structure.

Citrate makes much difference in the conformation of pure phase MFe_2O_4. Citrate has been widely used to provide monodisperse fine metal,[31−34] because of the high reducing capacity with a comparatively strong chelating ability. So in our synthesis, citrate can reduced part of Fe^{3+} to Fe^{2+} and coordinate with iron ions (Fe^{3+}or Fe^{2+}) to form stable complexes, whereas the synthesis of MFe_2O_4 (M = Co, Zn, and Mn), citrate directly coordinate with iron ions (Fe^{3+}or M^{2+}) to form stable complexes, which efficiently slow down reaction rate. Figure 6 describes the XRD patterns of Fe_3O_4 samples synthesized by different molars of citrate while keep

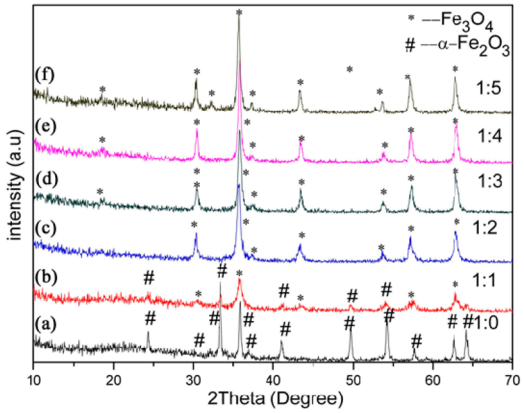

Figure 6. The XRD of Fe_3O_4 samples with different molar ratio of citrate/Fe^{3+}: 0:1 (a), 1:1 (b), 2:1 (c), 3:1 (d), 4:1 (e), and 5:1 (f).

other conditions consistent with typical reactions. From traces a to f, molar ratios of citrate/Fe^{3+} are 0:1, 1:1, 2:1, 3:1, 4:1, and 5:1, respectively, and we could see that without citrate the resultants were α-Fe_2O_3 (JCPDS Card No. 33-0664, trace a). Increasing the molar ratio of citrate/Fe^{3+} to 1:1, five peaks of Fe_3O_4 appeared (trace b), and corresponding morphology is shown in Figure S3a (See Supporting Information Figure S3 for SEM images of Fe_3O_4 synthesized at different molars ratios of citrate/Fe^{3+}, 1:1 (a), 3:1 (b), 4:1 (c), 5:1 (d), for the 2:1 molar ratio see Supporting Information Figure S2a). For the 2:1 molar ratio, the product is transformed to Fe_3O_4 totally (trace c), and the morphology is a sphere structure (Supporting Information Figure S2a). Further increasing the molar ratio to 3:1/4:1, product is still Fe_3O_4 nanospheres (trace d/e, Supporting Information Figure S3b/S3c). But the morphology of Fe_3O_4 (trace f) is irregular nanospheres (Supporting Information Figure S3d) for the high chelating ability of citrate after the molar ratio arrived at 5:1. In addition, excess citrate will influence the magnetism of ferrite.[35] Therefore, the optimum molar ratio of citrate/Fe^{3+} is from 2:1 to 4:1.

In a typical hydrothermal process, the diameters and shell thickness of MFe_2O_4 mesoporous nanospheres are influenced by the amount of CH_3COONa. Increasing the CH_3COONa dosage, the outer diameters of mesoporous ferrite nanospheres can decrease from 380 to 180 nm and the shell thickness decreases from 45 to 20 nm, but there could be little any effect on the sizes after the amount of CH_3COONa reaches to 13.5 mmol. Figure 7 shows the 180 nm (outer diameter) mesoporous ferrites hollow nanospheres synthesized by 13.5 mmol CH_3COONa (Fe_3O_4, Figure 7a; $CoFe_2O_4$, Figure 7b; $ZnFe_2O_4$, Figure 7c; and $MnFe_2O_4$, Figure 7d). As we all know, the large amount of CH_3COONa can sharply increase the OH^- concentration in the solution which can exceed the critical nucleation concentration, resulting in a homogeneous formation of nucleation.[36,37] The homogeneous nucleation increased the number of aggregation center in the solution which contain limited Fe^{3+} and M^{2+} and finally result in the formation of hollow nanospheres with small diameter.

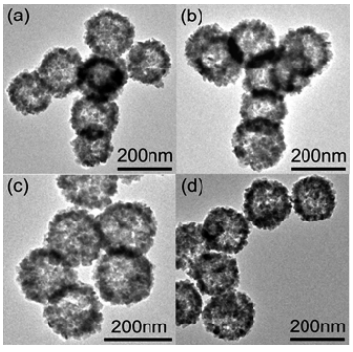

Figure 7. TEM images of Fe_3O_4 (a), $CoFe_2O_4$ (b), $ZnFe_2O_4$ (c), and $MnFe_2O_4$ (d).

Polyacrylamide [PAM] is a kind of neutral, nontoxic, hydrophilic and biocompatible polymer, which can improve the viscosity of the solution. The viscosity of mixture solution becomes greater once PAM is added into the mixture solution, and the friction force between primary nanoparticles becomes larger. Then the decreased viscosity will slow down the movement rate of primary nanoparticles and the increased friction force will maintain primary nannoparticles' structure, which give more time for the particles to aggregate into regular round spheres.[38] The controlled experiment indicated that without the presence of PAM, only irregular ferrite spheres were obtained, and little change on morphologies of the product appeared when the amount of PAM reaches 0.3 g. In order to show the difference between CH_3COONa and PAM to the morphology of products, we select the morphology of the ferrites represented by the of Fe_3O_4 hollow nanospheres. Figure 8a-c shows the SEM images of Fe_3O_4 hollow spheres

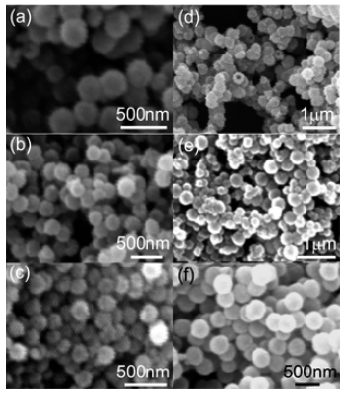

Figure 8. SEM images of Fe_3O_4 samples with different molar of CH_3COONa: 7.5 mmol (a), 10.5 mmol (b), and 13.5 mmol (c); and with different dosages of PAM: 0.075 g (d), 0.225 g (e), and 0.375 g (f).

obtained by different molar of CH_3COONa while other reaction conditions were the equivalent with those of typical manufacture. Figure 8d–f shows the SEM images of Fe_3O_4 hollow spheres obtained by different usage amount of PAM while other reaction conditions were the equivalent with those of typical manufacture. As shown in the Figure 8a–c, with the increase of the CH_3COONa, which changes from 7.5 to 13.5 mmol, outer diameters of the mesoporous ferrite nanospheres decrease from 290 to 180 nm. While in the Figure 8d-f changing the usage amount of PAM, outer diameters of the mesoporous ferrite nanospheres hardly vary (about 380 nm).

The morphology and structure of the products at various reaction time were examined by TEM and XRD to preliminarily understand the morphology and structure evolution of Fe3O4 hollow nanospheres, as shown in Supporting Information Figure S5 and S6. After the hydrothermal reaction of 2 h, only black turbid liquid was acquired,

indicating that the reaction rate was slow. After the hydrothermal reaction of 3 h the brown precipitation was obtained. The product was amorphous because of only glass peak found in the XRD pattern (Supporting Information Figure S5a). As shown in Supporting Information Figure S6a, the amorphous product composed of monodisperse solid nanospheres with diameters about 260 nm which were consisted of a large lot of primary nanoparticles. After the hydrothermal reaction of 4 h, the peaks belonged to spinel Fe_3O_4 presented to the XRD pattern of the as-obtained products (Supporting Information Figure S5b), indicating the commencement of crystallization. The diameter of solid nanospheres largened to 320 nm and the sizes of primary particles (especially the particles on the surface) obviously became larger (Supporting Information Figure S6b), After the hydrothermal reaction of 6 h, the crystalline of the as-obtained productions was largened (Supporting Information Figure S5c), meanwhile, it can be observed the nanospheres continued to grow large and there were some pale regions at interior of the spheres (Supporting Information Figure S6c), indicating the commence of evacuation. Further prolonging the reaction time to 12 h, the productions were translated to well-crystallized hollow nanospheres completely (Supporting Information Figures S5d and S6d). In a word, when prolonging the reaction time, the amorphous solid spheres were gradually transformed into well-crystallized hollow spheres and the diameters of the spheres had a trend to largen after the hollow nanospheres formed.

On the basis of outcomes of the control experiments, we propose that formation of the as-obtained ferrite undergoes two stages: (1) the formation of amorphous monodisperse solid spheres comprised of primary particles, (2) conversion between the solid spheres and hollow nanospheres. The formation process is illustrated in Supporting Information Figure S7.

In the first stage, the amorphous particles may first nucleate from the supersaturated solution, afterward, the new formed amorphous particles aggregate into nanospheres, stimulated by the minimization of total surface energy. In this stage, cooperative influences of citrate and PAM are critical for the formation of monodiseperse solid spheres. Their roles are interpreted as follows. For citrate, aside from its reducing properties, it also can be chelate with iron ions (Fe^{3+} or Fe^{2+}) to come into being steady complexes. The framework of complexes can sharply reduce the availability of free iron ions, as a result, the reaction rate changes slow which is momentous for the framework of well dispersed hollow nanospheres. The polymer PAM plays two roles in our synthesis system. On the one hand, PAM can work as a capping agent for stabilizer. Because of the large amount of amide ligands, PAM absorbed on the surface of the product consequently stabilizes the primary particles. At the same time, with the introduction of PAM, the viscosity of solution becomes greater. The increased viscosity will slow down the reaction rate as well as the movement rate of primary nanoparticles. And the slow movement rate allows primary nanoparticles to have enough time to aggregate into regular round spheres.

In the second stage, according to the observations from time-dependent experiments, we can clearly see the morphology evolution of as-obtained products experience a well-known Ostwald ripening process referring to a solution process in which the larger crystal grains form at the expense of the smaller ones. This whole process is illustrated in Supporting Information Figure S7. The amorphous solid spheres formed in the first stage grow continuously and start crystallizing at the surface of the spheres, because of the full contact between the surface and the solution. Finally, sizes of the constituent primary particles at the surface obviously become larger and their crystallinities become better. Compared with the large and well-crystallized particles on the exteriors of the spheres, the inner amorphous small crystallites have higher surface energy, which offers drive for the Ostwald ripening process. Then, the inner crystalltes tend to dissolve due to the existence of CH_3COONa, resulting in interior void space. The dissolved crystallites recrystallize on the exterior of spheres, which is confirmed by the fact that the diameters of the pheres increase with the reaction time. There is also a key problem needing to be resolved, which is how does the mass transportation occur? Here, two points can ensure the occurrence of mass transportation. First, the pores on the spheres (confirmed by the BET analysis above) provide the channels for the mass transportation. Second, the strong coordinating ability of citrate and CH_3COONa promotes the dissolution of Fe_3O_4, which can generate the necessary ionic transportation in the ripening process.[22]

To study the maximum adsorption capacity of ferrite (MFe_2O_4, M = Fe, Co, Zn, and Mn) hollow nanospheres, we selected the hollow nanospheres for the object of study, whose diameter is 380 nm, and carried out the adsorption experiments. Adsorption kinetic investigation (Figure 9) had been performed under pH 5 at different time intervals, where the initial As(V) and Cr(VI) ions concentration is 8000 μg/L. On the basis of the outcomes of adsorption kinetic investigation, it has a great start adsorption rate, and until 20 h the variation curve almost linearly changes. When the agitation time was prolonged to 40 h, the system reached to equilibrium. According to the adsorption batch tests of Experimental Section, we can calculate that the As(V) and Cr(VI) ions adsorption isotherms matched well with Langmuir model, exhibiting high adsorption capacity of 350 mg/g, totally. As a comparison, example for Cr(VI) ion, we selected the Fe_3O_4 hollow nanospheres for the object of study, and carried out the adsorption experiments, where we kept the other conditions constant. Adsorption kinetic investigation (Supporting Information Figure S8) had been performed. Based on the outcomes of adsorption kinetic investigation, it has a great start

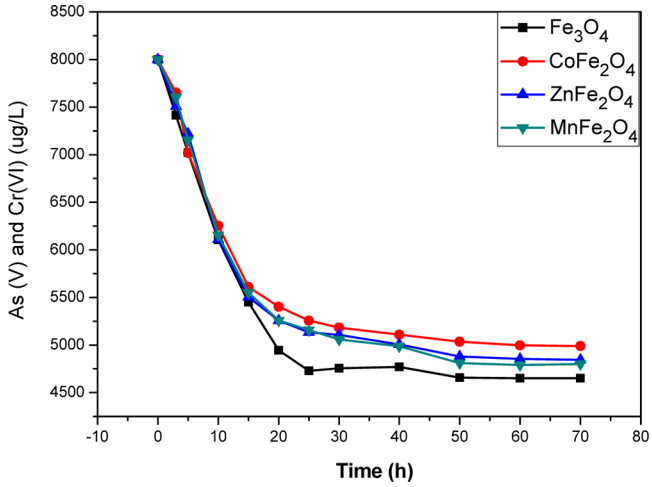

Figure 9. Adsorption kinetics of ferrites (MFe_2O_4; M = Fe, Co, Zn, and Mn) under pH 5.

adsorption rate, and until 10 h the variation curve almost linearly changes. When the agitation time was prolonged to 15 h, the system reached to equilibrium. We can calculate that adsorption isotherms of Cr(VI) ion exhibited high adsorption capacity of 230 mg/g, indicating that the As(VI) adsorption capacity of Fe_3O_4 should be higher than 110 mg/g.

EDS from individual Fe_3O_4 nanosphere analysis was also measured to show the condition of As(V) and Cr(VI) ions absorbed on nanospheres, after which has been carried out the adsorption experiments, where the initial concentration is 2 M (Supporting Information Figure S9a for As(V) ion, Supporting Information Figure S9b for Cr(VI) ion, Supporting Information Figure S9c for As(V) and Cr(VI) ions). Besides the C peaks which come from the copper grids, only As, Fe, and O peaks (Supporting Information Figure S9a), Cr, Fe, and O peaks (Supporting Information Figure S9b), As, Cr, Fe, and O peaks (Supporting Information Figure S9c) for Fe_3O_4 after carried out the adsorption experiments, indicating that the As(V) and Cr(VI) ions have been adsorbed on magnetic nanospheres.

As we know, pH have a significant effect on As(V) and Cr(VI) ions adsorption. Therefore, it is essential to investigate the effect of initial pH values on the adsorption of As(V) and Cr(VI) ions. Figure 10 shows the effect of pH on As(V) and

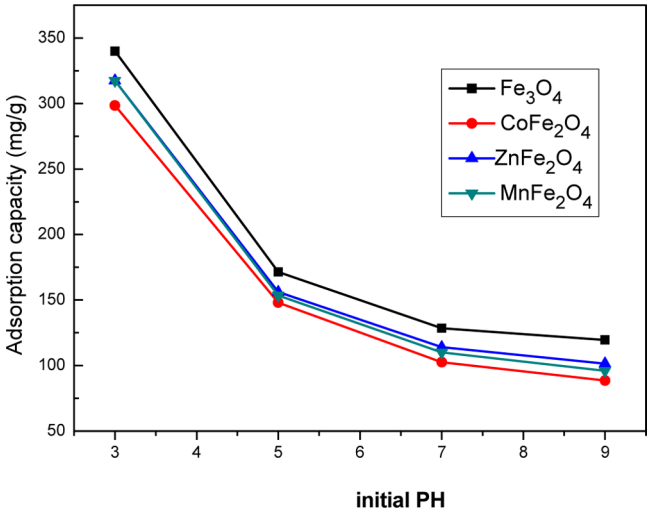

Figure 10. Effect of pH on adsorption capacity with initial As(V) and Cr(VI) [As(V) + Cr(VI)] on centration of 8000 μg/L.

Cr(VI) ions adsorption ability, we could see the stronger the acidity of wastewater is, the higher the adsorbent capacity will be. As Figure 10 shows, the maximal adsorption capacity is about 350 mg/g, and the number is equal to that of Figure 9. For studying the maximum adsorption capacity of MFe_2O_4, the graphs of four as-obtained adsorption isotherms at pH 3 are shown in Figure 11, the equilibrium could be obtained in all adsorption isotherms, Fe_3O_4 hollow nanospheres possesses the highest As(V) and Cr(VI) ions adsorption ability of 340 mg/g, which is approximately equal to that of Figure 9, followed by $ZnFe_2O_4$ (318 mg/g), $MnFe_2O_4$ (316 mg/g), and $CoFe_2O_4$ (299 mg/g) hollow nanospheres, when the equilibrium As(V) and Cr(VI) solution concentration approximately reach to 7000 μg/L. The adsorption equilibrium curve consists of two components langmuir curve, example for Fe_3O_4, where at low concentrations (<2000 μg/L), the adsorption isotherm is consistent with the simple langmuir curve, whose maximum adsorption capacity is 86 mg/g; while at high concentrations

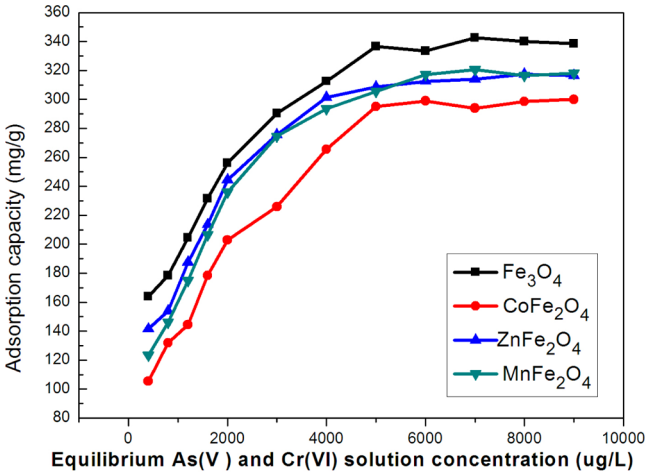

Figure 11. As(V) and Cr(VI) [As(V) + Cr(VI)] uptake capacity of ferrites hollow nanospheres under pH 3.

(>2000 μg/L), the adsorption isotherm curve has some deviation with the simple langmuir, but consistent with the secondary langmuir curve, whose maximum adsorption capacity is 340 mg/g, which is relate to the as-prepared hollow nanospheres. Theoretically, the maximum adsorption values based on surface area for all four ferrites should be similar, the different adsorption capacities between these four ferrites is offered to relate to surface complexation and ion exchange between the ferrites surface and the As(V) and Cr(VI) ions in solution. There is a kind of surface complexation generated between the As(V) and Cr(VI) ions and those irregular primary nanoparticles (the diameter of ~15 nm), of which the hollow sphere is loosely composed. And the adsorption for As(V) and Cr(VI) ions resulted from the ion exchange between the As(V) and Cr(VI) ions and these irregular primary nanoparticles, which results in the large adsorption capacity of our Fe_3O_4 hollow nanospheres. In comparison, it is clear that the ferrites hollow nanospheres have a higher adsorption value than other nanoparticles.[39] The excellent absorption capacity can be put down to the well hollow structure, good specific surface area, high-quality monodisperse, and high magnetic saturation of the prepared ferrites.

A straightforward regeneration investigation was carried out to analyze recycle properties of the As(V) and Cr(VI) ions absorption for the synthesized MFe_2O_4 hollow microspheres. The recycle capacity of MFe_2O_4 hollow nanospheres were measured, adopting NaOH solution to displace the adsorbed As(V) and Cr(VI). We can see the adsorption capacity of magnetic hollow nanospheres is 255 mg/g in the fifth recycle (Supporting Information Figure S10), which becomes 75% of initial adsorption capacity (340 mg/g), however, the adsorption capacity of that is only 169 mg/g in the sixth cycle, which becomes 50% of the initial adsorption capacity. The outcome illuminates the as-obtained magnetic hollow nanospheres could serve as an outstanding rebirth As(V) and Cr(VI) ions adsorbent within the fifth cycle, due to that As(V) and Cr(VI) ions adsorption on magnetic microspheres contained a reversibly physical process, which is electrostatic attraction and an irreversible redox. It is well-known the adsorption capacity of magnetic nanospheres for As(V) and Cr(VI) ions is effected by the As(V) and Cr(VI) ions concentration.[40]

CONCLUSIONS

Hydrothermal route was adopted to successfully synthesize the magnetic MFe_2O_4 (M =Fe, Co, Zn, and Mn) hollow nanospheres. The manufactured processes shown in the work provide several very significant advantages over the routine measures. First, the diameter of mesoporous ferrites nanospheres could be tuned from 380 to 180 nm, when the amount of CH_3COONa is changed. Second, this hydrothermal method is generalized progress that may be spreaded to the controlled fabrication of other metal oxides with similar morphologies. Third, the synthetic method is friendly for environment, simply and economical, because it adopts innoxious progress and inexpensive reactants. In particular, 380 nm ferrites hollow spheres exhibit a adsorption capacity as high as 340 mg/g. Taking into account the suitable size, large hollow structure, large pore volume, exceptional adsorption for As(V) and Cr(VI) ions, strong magnetic response, good hydrophilic properties, and well biocompatible properties, the mesoporous ferrite hollow nanospheres will be an ideal candidate in biomedical and environmental processing fields.

ASSOCIATED CONTENT

Supporting Information

EDS for Fe_3O_4 (a), $CoFe_2O_4$ (b), $ZnFe_2O_4$ (c), and $MnFe_2O_4$ (d), SEM images of the as-prepared Fe_3O_4 (a), $CoFe_2O_4$ (b), $ZnFe_2O_4$ (c), and $MnFe_2O_4$ (d), SEM images of Fe_3O_4 obtained at different molars ratios of citrate/Fe^{3+}, 1:1 (a), 3:1 (b), 4:1 (c), 5:1 (d), for the 2:1 molar ratio see Figure S1a, N_2 adsorption−desorption isotherm (a) and pore size distribution curve (b) of the magnetite hollow spheres, XRD patterns of the products obtained at different reaction times: (a) 3 h, (b) 4 h, (c) 6 h, (d) 12 h with other conditions were the same as the typical synthesis, TEM images of the products obtained at different reaction times: (a) 3 h, (b) 4 h, (c) 6 h, (d) 12 h where other conditions were the same as the typical synthesis, schematic illustration of the formation of magnetite hollow spheres: ripening starts at the center of the spheres, resulting in the formation of hollow spheres, adsorption kinetics of Fe_3O_4 hollow nanospheres for Cr(VI) ion under pH = 5, EDS from individual Fe_3O_4 nanosphere analysis after been carried out the adsorption experiments, where the initial concentration of As(V) ion is 2 M (a), the initial concentration of Cr(VI) ion is 2 M (b), and the initial concentration of As(V) and Cr(VI) ions is 2 M (c), respectively, and reusability of the MFe_2O_4 hollow microspheres. This material is available free of charge via the Internet at http://pubs.acs.org.

AUTHOR INFORMATION

Corresponding Author

*Tel:+86-378-2868833-3712. Fax:+86-378-3881358. E-mail: smzhou@henu.edu.cn.

Notes

The authors declare no competing financial interest.

ACKNOWLEDGMENTS

The study was sectionally sustained by the Program for Science & Technology Innovation Talents in Universities of Henan Province (No.2008 HASTIT002), Innovation Scientists and Technicians Troop Construction Projects of Henan Province (No.094100510015), and the Natural Science Foundation of China under Grant No. 20971036.

REFERENCES

(1) Caruso, F.; Caruso, R. A.; Mohwald, H. *Science* **1998**, *282*, 1111−1114.
(2) Wu, X.; Lu, G. Q. M.; Wang, L. *Energy Environ. Sci.* **2011**, *4*, 3565−3572.
(3) Du, J.; Qi, J.; Wang, D.; Tang, Z. *Energy Environ. Sci.* **2012**, *5*, 6914−6918.
(4) Xu, H.; Wang, W. *Angew. Chem., Int. Ed.* **2007**, *46*, 1489−1492.
(5) Ye, Q. L.; Yoshikawa, H.; Bandow, S.; Awaga, K. *Appl. Phys. Lett.* **2009**, *94*, No. 063114.
(6) Li, B.; Rong, G.; Xie, Y.; Huang, L.; Feng, C. *Inorg. Chem.* **2006**, *45*, 6404−6410.
(7) Graf, C.; Dembski, S.; Hofmann, A.; Ruhl, E. *Langmuir* **2006**, *22*, 5604−5610.
(8) Yang, H. G.; Zeng, H. C. *J. Phys. Chem. B* **2004**, *108*, 3492−3495.
(9) Cao, X. B.; Gu, L.; Zhuge, L. J.; Gao, W. J.; Wang, W. C.; Wu, S. F. *Adv. Funct. Mater.* **2006**, *16*, 896−902.
(10) Lou, X. W.; Wang, Y.; Yuan, C.; Lee, J. Y.; Archer, L. A. *Adv. Mater.* **2006**, *18*, 2325−2329.
(11) Klas, S.; Dubowski, Y.; Lahav, O. *J. Hazard. Mater.* **2011**, *193*, 59−64.
(12) Hyeon, T. *Chem. Commun.* **2003**, *8*, 927−934.
(13) Li, K.; Peng, C.; Jiang, K. *J. Hazard. Mater.* **2011**, *194*, 79−84.
(14) Zhang, D.; Tong, Z.; Li, S.; Zhang, X.; Ying, A. *Mater. Lett.* **2008**, *62*, 4053−4055.
(15) Hu, P.; Yu, L.; Zuo, A.; Guo, C.; Yuan, F. *J. Phys. Chem. C* **2008**, *113*, 900−906.
(16) Caruso, F.; Spasova, M.; Susha, A.; Giersig, M.; Caruso, R. A. *Chem. Mater.* **2001**, *13*, 109−116.
(17) Lee, J. E.; Yu, S. H.; Lee, D. J.; Lee, D. C.; Han, S. I.; Sung, Y. E.; Hyeon, T. *Energy Environ. Sci.* **2012**, *5*, 9528−9533.
(18) Chen, Y.; Xia, H.; Lu, L.; Xue, j. *J. Mater. Chem.* **2012**, *22*, 5006−5012.
(19) Wang, B.; Chen, J. S.; Wu, H. B.; Wang, Z.; Lou, X. W. *J. Am. Chem. Soc.* **2011**, *133*, 17146−17148.
(20) Liu, S.; Xing, R.; Lu, F.; Rana, R. K.; Zhu, J. J. *J. Phys. Chem. C* **2009**, *113*, 21042−21047.
(21) Zhu, L. P.; Xiao, H. M.; Zhang, W. D.; Yang, G.; Fu, S. Y. *Cryst. Growth Des.* **2008**, *8*, 957−963.
(22) Cheng, W.; Tang, K.; Qi, Y.; Sheng, J.; Liu, Z. *J. Mater. Chem.* **2010**, *20*, 1799−1805.
(23) Zeng, Y.; Yao, J.; Horri, B. A.; Wang, K.; Wu, Y.; Li, D.; Wang, H. *Energy Environ. Sci.* **2011**, *4*, 4074−4078.
(24) Yuan, H. L.; Wang, Y. Q.; Zhou, S. M.; Lou, S. Y. *Chem. Eng. J.* **2011**, *175*, 555−560.
(25) Yuan, H. L.; Wang, Y. Q.; Zhou, S. M.; Liu, L. S.; Chen, X. L.; Lou, S. Y.; Yuan, R. J.; Hao, Y. M.; Li, N. *Nanoscale Res. Lett.* **2010**, *5*, 1817−1821.
(26) Rath, C.; Anand, S.; Das, R. P.; Sahu, K. K.; Kulkarni, S. D.; Date, S. K.; Mishra, N. C. *J. Appl. Phys.* **2002**, *91*, 2211−2215.
(27) Syue, M. R.; Wei, F. J.; Chou, C. S.; Fu, C. M. *J. Appl. Phys.* **2011**, *109*, No. 07A324.
(28) Li, G.; Zhao, Z.; Liu, J.; Jiang, G. *J. Hazard. Mater.* **2011**, *192*, 277−283.
(29) Liu, X.; Kaminski, M. D.; Guan, Y.; Chen, H.; Liu, H.; Rosengart, A. J. *Magn. Magn. Mater.* **2006**, *306*, 248−253.
(30) Absalan, G.; Asadi, M.; Kamran, S.; Sheikhian, L.; Goltz, D. M. *J. Hazard. Mater.* **2011**, *192*, 476−484.
(31) Huang, T.; Xu, H. N. *J. Mater. Chem.* **2010**, *20*, 9867−9876.
(32) Xiong, Y.; McLellan, J. M.; Yin, Y.; Xia, Y. *Angew. Chem., Int. Ed.* **2007**, *119*, 804−808.
(33) Chen, D.; Mei, C. Y.; Yao, L. H.; Jin, H. M.; Qian, G. R.; Xu, Z. P. *J. Hazard. Mater.* **2011**, *192*, 1675−1682.
(34) Ji, X. H.; Song, X. N.; Li, J.; Bai, Y. B.; Yang, W. S.; Peng, X. G. *J. Am. Chem. Soc.* **2007**, *129*, 13939−13948.
(35) Liu, J.; Sun, Z. K.; Deng, Y. H.; Zou, Y.; Li, C. Y.; Guo, X. H.; Xiong, L. Q.; Gao, Y.; Li, F. Y.; Zhao, D. Y. *Angew. Chem.* **2009**, *121*, 5989−5993.

(36) Liu, R.; Zhao, Y.; Huang, R.; Zhao, Y.; Zhou, H. *Eur. J. Inorg. Chem.* **2010**, *2010*, 4499−4505.
(37) Gao, Q.; Zhang, J.; Hong, G.; Ni, J. *J. Nanosci. Nanotechnol.* **2010**, *10*, 6400−6406.
(38) Wang, G.; Sæterli, R.; Rørvik, P. M.; Helvoort, A. T.; Holmestad, R.; Grande, T.; Einarsrud, M. A. *Chem. Mater.* **2007**, *19*, 2213−2221.
(39) Mayo, J. T.; Yavuz, C.; Yean, S.; Cong, L.; Shipley, H.; Yu, W.; Falkner, J.; Kan, A.; Tomson, M.; Colvin, V. L. *Sci. Tech. Adv. Mater.* **2007**, *8*, 71−75.
(40) Liu, Y. B.; Wang, Y. Q.; Zhou, S. M.; Lou, S. Y.; Yuan, L.; Gao, T.; Wu, X. P.; Shi, X. J.; Wang, K. *ACS Appl. Mater. Inter.* **2012**, *4*, 4913−4920.